Evidence That Strain-Rate Softening Is Not Necessary for Material Instability Patterns

Julio R. Valdes, François Guillard, and Itai Einav

Phys. Rev. Lett. **119**, 118004 — Published 15 September 2017

DOI: 10.1103/PhysRevLett.119.118004

Evidence that strain-rate softening is not necessary for material instability patterns

Julio R. Valdes*
Geo-Innovations Research Laboratory, Department of Civil, Construction, and Environmental Engineering, San Diego State University, San Diego, California 92182, USA.

François Guillard and Itai Einav†
Particles and Grains Laboratory, School of Civil Engineering, The University of Sydney, Sydney, New South Wales 2006, Australia
(Dated: July 25, 2017)

Strain-rate softening has been associated with a wide variety of material instabilities, from the Portevin – Le ~~Châtelier~~Chatelier effect in metal alloys to stick-slip motion in crust faults. Dynamic instability patterns have been recently discovered in brittle porous media: diffused, oscillatory, and erratic compaction. ~~Using experiments with puffed rice and model simulations~~Using model simulations inspired by experiments with puffed rice, we question the link between these dynamic patterns and strain-rate sensitivity in such media. An important feature of our model is that it can recover strain-rate softening as an emergent phenomenon, without imposing it *a priori* at its microstructural scale. More importantly, the model also demonstrates that the full range of dynamic patterns can develop without presenting macroscopic strain-rate softening. Based on this counter example model we therefore argue that strain-rate softening should not be ~~seen~~taken as a necessary condition for the emergence of instability patterns. Our findings in brittle porous media have implications on models that require strain-rate softening to explain earthquake and metal alloy instabilities.

PACS numbers: Valid PACS appear here

Studying the compaction behavior of common brittle porous materials such as sandstone presents experimental difficulties due to the large pressures and timescales over which compaction occurs [1, 2]; i.e., up to millions of years. These issues inspired the choice of puffed rice cereal as an analogous material for compression testing [3, 4]. Indeed, cereal grains are highly porous, brittle, and compliant, and their compaction behavior can be studied on a small scale within a small time-frame, suitable for laboratory experiments (Fig. 1a). Initial experiments revealed unexpected and surprising results, i.e., oscillatory compaction: a compaction band propagates periodically, opposite to the direction of loading, and faster than the imposed shortening rate [3]. Inspired by model simulations, later experiments disclosed a variety of other compaction patterns, such as erratic and diffuse [4]. These discoveries have opened a new field of research into 'crunchy matter' [5], i.e., porous, brittle media, composed predominantly of voids. Since then, similar compaction patterns have been witnessed in snow [6].

Bifurcated deformations in solid media are common: from dislocations of impurities in alloys, to non-uniformly propagating fractures in fibrous and brittle media, to stick-slip motions in crust faults. The manifestation of these processes has long been associated with strain-rate softening, where the observed bulk stress increases with decreasing strain-rate. A typical example is the Portevin – Le ~~Châtelier~~Chatelier (PLC, [7]) effect in metal alloys, which has been linked to dynamical aging of dislocations with impurity atoms [8–14]. The PLC effect is commonly explained through the use of continuum constitutive models that incorporate phenomenological strain-rate softening at low rates followed by hardening at high rates. Quite similarly, bifurcated stick-slip motions in fault gouges have been described through so-called 'rate and state friction' phenomenological models [15–19], and oscillatory, transient, and chaotic bifurcated motions associated with fractures in polymeric and amorphous brittle materials have been explained using a velocity-stress relationship (at the fracture tip) that also obeys a velocity-softening law [20].

We question whether strain-rate softening, as has been observed experimentally at the bulk sample scale in snow [6, 21, 22], is a necessary condition for obtaining dynamic instability patterns in brittle porous media. To address this point, we seek a model that can capture strain-rate softening as an emergent phenomenon from microstructural properties. Towards these aims we present new experiments on puffed rice cereal and simulations with a spring-lattice model [4], both revealing pronounced strain-rate softening along with bifurcated patterns.

The stress response of brittle porous media is highly sensitive to the imposed compaction velocity V, as shown in Fig. 1b [23], where each curve denotes the stress sustained (right ordinate) during uniaxial shortening of a pack of cereal grains housed inside a cylindrical acrylic die with diameter about 35 times larger than a single grain (Fig. 1a). Curves are deliberately offset by 50 kPa to enable visual comparisons. Corresponding values of scaled stress are also shown (left ordinate), where stresses are scaled by the constrained modulus M of a puffed rice

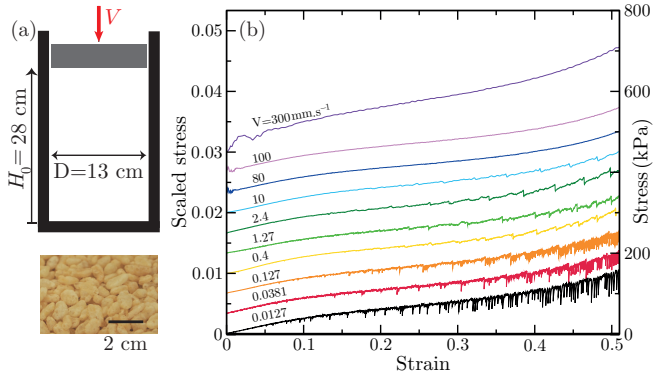

FIG. 1. Constant velocity experiments (a) Experimental device and puffed rice. (b) Stress-strain curves for various compaction velocities. Each curve is offset 50 kPa from the previous one for clarity. Left ordinate: stress scaled by the typical constrained modulus of the puffed rice, 15MPa.

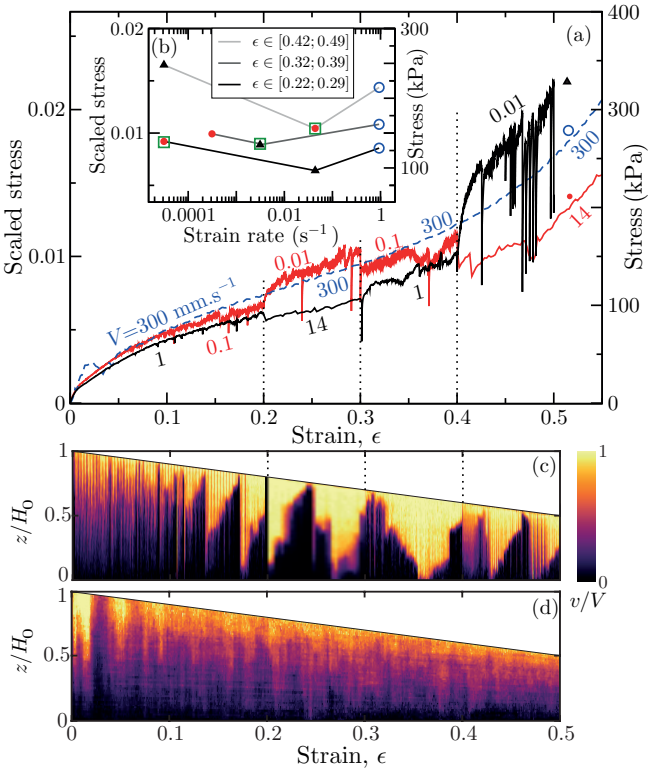

FIG. 2. Variable velocity experiments. (a) Stress-strain curves for variable velocity tests (full lines), and a constant velocity test (dotted line). (b) Stress averaged over three different strain bins for variable velocity tests and constant velocity test at highest velocity ($V = 300\,\mathrm{mm.s^{-1}}$). ▲, ●, □ are variable velocity tests, the first two are shown in (a); ○ is constant high velocity test, also shown in (a). Corresponding scaled stresses in (a-b) are also shown, where stress values are scaled by the typical constrained modulus of the material. (c) Velocity field for the variable velocity test that corresponds to the black line in (a). (d) Velocity field for the constant velocity test that corresponds to the blue line in (a).

pack under low static stress. $M = 15\,\mathrm{MPa}$ was calculated via p-wave propagation velocity measurements using piezoelectric sensors placed on opposite ends of the pack. All curves show serrations overlaid over otherwise strain-hardening trends; such being remarkably similar for all tests, despite the difference in V. The serration amplitudes, i.e., stress drops, however, decrease with increasing V, much like PLC serrations [9–11, 13]. The curves for $V \leq 0.13\,\mathrm{mm.s^{-1}}$ show stress drops that "fall off" the trend, with fluctuations that seldom rise diminutively above the trend. These serrations are reminiscent of type C PLC serrations [24–26], which are produced by the nucleation of static localized deformation bands. In contrast, curves between $V = 1.3$ and $10\,\mathrm{mm.s^{-1}}$ exhibit (i) a pronounced periodicity of large serrations, (ii) many small serrations between large ones, and (iii) stresses that fluctuate around the general trend. These serrations are similar to type A and type B PLC serrations, which emerge due to different PLC kinetics, yet are similar in that both are associated with the propagation of localized deformation bands [26]. Our tests with $V \geq 80\,\mathrm{mm.s^{-1}}$ render very small stress drops; largely indiscernible when compared to those for $V < 80\,\mathrm{mm.s^{-1}}$ and not readily comparable to any of the PLC serration types.

Similarities in the serrations exhibited by brittle matter and alloys prompted us to examine if the macroscopic stress supported by crunchy matter during compaction is strain-rate sensitive. Overlaying the stress curves in Fig 1b led to difficulties in unraveling strain rate sensitivity features because the stress level at a given strain depends strongly on the initial conditions of the pack, namely the pack density and the strength and stiffness of the grains, which inevitably vary between samples. We solved this caveat by conducting variable velocity tests: we compressed each specimen in four sequential stages, each stage with a different V. The results of two variable velocity tests are shown in Fig. 2a, together with a constant high-velocity test. Note that each of these packs exhibits significant strain rate sensitivity, as evidenced by hardening upon a decrease in strain rate, and softening upon an increase in strain rate. We quantified the strain rate sensitivity by averaging the stresses measured over selected strain ranges, for each experiment, and comparing them in Fig. 2b. We note that the stress measured for any given V is remarkably similar across experiments, regardless of the loading sequence, for a given strain range. We also note that at high strain rates, strain hardening behavior is recovered; in this case, the piston compresses the pack faster than the speed with which the grains break.

The serrations shown in Figs. 1 and 2a are associated with deformation features within each pack. To access such features, we filmed the deformation of each pack and employed digital image correlation (DIC) to create a spatiotemporal map of local vertical velocities from the

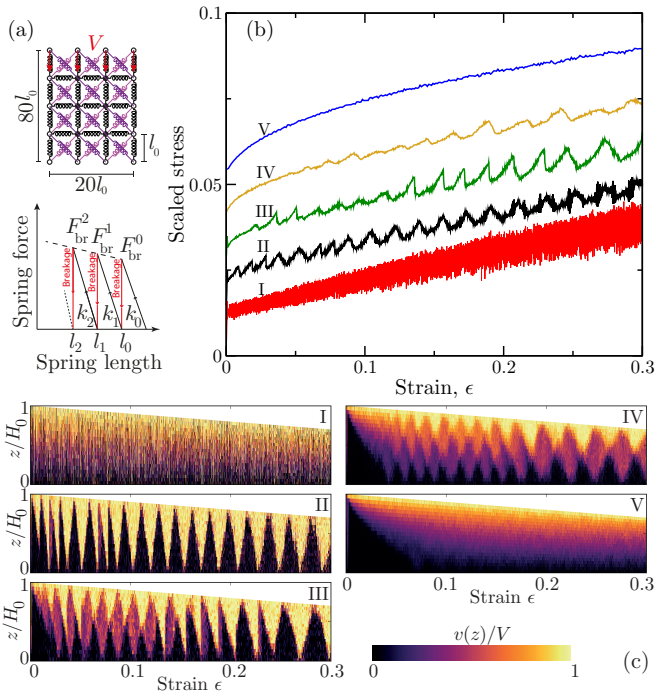

FIG. 3. Spring-lattice model. (a) Lattice configuration (top) and spring force-displacement law (bottom) used for the simulations. (b) Stress scaled by the theoretical initial modulus ($\frac{1+\sqrt{2}}{l_0}k_0$) as a function of strain, for different constant velocity tests with $V = \{5\cdot10^{-6}, 2\cdot10^{-5}, 4\cdot10^{-5}, 8\cdot10^{-5}, 1.6\cdot10^{-4}\}$ using $k_0 = 0.004$, $F_{\rm br} = 4\cdot10^{-6}$, $\eta = 0.002$, $a = 0.01$. (c) Spatiotemporal vertical velocity fields, with symbols I–V that correspond to lines in (b) and data points in Fig. 4.

gathered frames, as follows [3]. The full velocity field is first extracted by correlating consecutive images at time t, and the velocity v measured for locations at the same height z are averaged given the system's radial symmetry, which also leads to velocities that are only vertical. Finally, the field $v(z,t)$ is plotted as a colormap as in Figs. 2c-d.

Spatiotemporal maps associated with a variable velocity test (black curve in Fig. 2a), and the $V = 300\,\mathrm{mm.s^{-1}}$ test (dashed curve in Fig. 2a) are shown in Fig. 2c and 2d, respectively. Fig. 2c reveals that the compaction pattern transitions in accordance to the strain rate: localized compaction band propagation occurs at medium rates (e.g., $V = 1$ mm/s for $0.1 \lesssim \epsilon < 0.2$ and $0.3 < \epsilon < 0.4$), and traces of erratic compaction are observed when the rate is low (e.g., $V = 0.01$ mm/s for $\epsilon > 0.4$). At the high rate, the edges of the compaction bands are more diffuse ($0.2 < \epsilon < 0.3$). The map of the constant rate test reveals the diffused pattern of compaction that manifests as the material compacts quasi-homogeneously. These patterns are consistent with our previous observations [4].

The variability in the packing and material properties of puffed rice results in limited reliability to quantitatively assess the strain-rate softening properties of the material. Indeed, although experiments conducted with a given velocity display similar compaction patterns, the variability of the measured stress for experiments with the same V is of the same order as that of the change in stress when the velocity is modified. The implementation of continuous compression at a very slow velocity – so as to explore a quasi-static response – was also experimentally difficult with our loading system. For these reasons, we performed simulations with a two-dimensional lattice model of crushable springs, which was proven highly applicable to brittle porous media [4] (Fig. 3a). In this model, each node of mass m in a square lattice is linked to its eight neighbors by springs that are able to break when the force in the spring reaches a threshold force $F^{\rm br}$. The lowest lattice nodes are fixed, the uppermost nodes move at constant velocity V, and the side nodes are constrained to move only vertically. When a spring breaks, its equilibrium length shortens, and its stiffness k and strength $F_{\rm br}$ are increased: $k \to k + ak_0$, $F^{\rm br} \to F^{\rm br} + aF^{\rm br}_0$, where k_0 and $F^{\rm br}_0$ are the initial stiffness and strength respectively, and $a = 0.01$ is a constant. The equation of motion of each node is solved by a Verlet algorithm with timestep Δt, and the force on each node is given by the forces created by the spring and by a viscous damping on the node, proportional to its velocity with damping coefficient η. The simulations are non-dimensional, with unit mass $[M] = m$, unit time $[T] = \Delta t$ and unit length $[L] = l_0$ for the initial lattice pitch. All the nodes and springs have the same properties.

Fig. 3b shows the macroscopic stress as a function of strain at the top of the crushable spring lattice. Qualitatively, the various serration patterns observed experimentally in Fig. 1b are recovered through the simulations, with numerous noisy stress drops at low compaction velocities, large coherent stress oscillations at intermediate compaction velocities, and an essentially smooth stress evolution with time at larger compaction velocities. There are, however, some differences. In the experiments, large serrations arise only after a certain strain level: during initial loading a real sample first suffers some grain rearrangement before sustaining significant breakage. Conversely, the lattice is inherently arranged and thus susceptible to breakage shortly after loading. In addition, the differences in the frequency of the serrations at low V are most likely due to the fact that high frequency fluctuations are filtered by the sampling rate and dynamics of the experimental measurement system (this is not the case in the simulations). These phenomenological differences at low V may result due to synchronization in spring-lattice models [27], and would deserve further study using statistical methods developed for analyzing PLC type C serrations [28]. Note that irrespective of these differences, neither the experiments nor the simulations exhibit coherent compaction bands at low velocities.

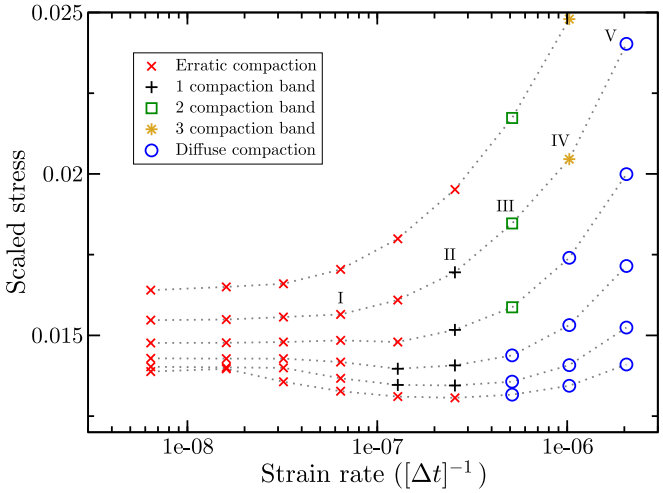

FIG. 4. Scaled stress as a function of strain rate, measured in strain range $\epsilon \in [0.01, 0.05]$. All simulations have $k_0 = 0.004$, $F_{\rm br} = 4 \cdot 10^{-6}$. The different dotted lines correspond to different viscosities, from bottom to top $\eta = \{1.25 \cdot 10^{-4}, 2.5 \cdot 10^{-4}, 5 \cdot 10^{-4}, 0.001, 0.002, 0.004\}$. Data points denoted I-V correspond to simulations shown in Fig. 3.

These different stress-time phenomena can be directly related to the compaction patterns that evolve through the lattices. Fig. 3c shows the spatiotemporal velocity maps that correspond to the various stress-strain curves in Fig. 3b. The large stress serrations at low V correspond to the essentially erratic compaction velocity field in Fig. 3cI, where the sample breaks at random locations over time. In contrast, the smooth stress curves observed under higher velocities correspond to a homogeneous and diffused compaction of the sample (Fig. 3cV). Finally, the large stress oscillations at intermediate velocities are directly related to the propagation of respectively one, two or three oscillatory compaction bands, which essentially split the samples into two, three or four zones that move nearly as rigid bodies with different velocities (resp. Fig. 3cII to 3cIV).

To quantitatively compare the simulated and experimental stress, we scale the simulated stress by the theoretical initial modulus of the lattice $\frac{1+\sqrt{2}}{l_0}k_0$. The scaled stress is of the same order of magnitude as the one obtained in the experiments, showing that the simulations and the experiments can be compared meaningfully both in terms of their compaction behavior and typical pressures. The qualitative differences in the shape of the curves could be explored in the future by introducing randomness in model properties and spring hardening.

One advantage of the current crushable spring-lattice model over the experiments is that there is no randomness in material properties. We exploit this deterministic feature of the model to accurately evaluate characteristic stresses that correspond to different strain-rates; clearly, this is difficult to achieve experimentally due to inevitable initial material variability. Fig. 4 shows the characteristic stress averaged in a given strain range $\epsilon \in [0.01, 0.05]$, for different strain-rates and viscosities, with symbols ($\times$, $+$, $\square$, $*$, $\circ$) that denote distinct compaction patterns. Simulations with low viscosities clearly show macroscopic strain-rate softening at intermediate strain-rates, followed by strain-rate hardening. For example, for simulations with $\eta = 2.5 \cdot 10^{-4}$, strain-rate softening occurs under macroscopic strain-rates from $\sim 3 \cdot 10^{-8}$ to $\sim 2 \cdot 10^{-7}$. Importantly, this softening is an emergent property of the model, which does not impose it at its microscale (i.e., there is only a rate independent force-displacement law for the springs and viscous hardening for the damping of the nodes). In this example of $\eta = 2.5 \cdot 10^{-4}$, the oscillatory compaction pattern appears under strain-rates that correspond to the strain-rate softening regime. This relation is consistent with observations of moving PLC patterns in alloys [13, 26].

A key question is whether such forms of material instability are always strictly linked with strain-rate softening. Indeed, we notice that macroscopic strain-rate softening vanishes for viscosities higher than ~ 0.001; yet, the full range of instability patterns is still realized. Specifically, the five simulations I-V in Fig. 3 for $\eta = 0.002$ are presented in Fig. 4, where the scaled stress always hardens with strain-rate. We note that the instability patterns that occur during rate-hardening, as shown in simulations II, III, and IV, exhibit serrations that resemble both type A and type B PLC serrations, as well as the serrations observed during the intermediate velocity experiments ($V = 0.4$ to 10 mm.s^{-1}). ~~This conclusion~~The finding of instabilities during rate-hardening is confirmed in Supplementary Material to be independent on the way the model dissipates energy, by replacing the dashpots at the mass nodes with Kelvin-Voigt's spring-dashpots between neighboring nodes. The implications of these two counter examples is that strain-rate softening should not be taken as a necessary condition for such material instabilities. Besides breakage, additional processes such as inter-granular adhesion may also be relevant. Granular breakage, however, controls the compression dynamics of brittle puffed rice packs.

In summary, using new experiments and model simulations we discussed the links between propagating instabilities in brittle porous media and strain-rate softening. Experimentally, we revealed both strain-rate softening and propagating compaction bands in compacted puffed rice. Numerically, using a simple crushable spring-lattice model, we were then able to reproduce this phenomenon of macroscopic strain-rate softening without imposing strain-rate softening *ad hoc* at the lower scales. Furthermore, we also show that all the compaction pattern types can emerge without any strain-rate softening. This latter example has implications beyond modeling brittle porous media, and challenges the imposition of strain-rate softening to explain material instabilities, for example, the

PLC effect in alloys and stick-slipping in crustal faults.

ACKNOWLEDGMENT

The authors acknowledge the United States National Science Foundation (CBET 1336952) and the Australian Research Council (DP130101291 and DP160104310) for funding.

* jvaldes@mail.sdsu.edu
† Department of Civil, Environmental & Geomatic Engineering, Faculty of Engineering Science, University College London, London WC1E 6BT, UK.

[1] J. Rudnicki and J. Rice, Journal of the Mechanics and Physics of Solids **23**, 371 (1975).
[2] W. A. Olsson, Journal of Geophysical Research: Solid Earth **104**, 7219 (1999).
[3] J. R. Valdes, F. L. Fernandes, and I. Einav, Granular Matter **14**, 71 (2012).
[4] F. Guillard, P. Golshan, L. Shen, J. Valdes, and I. Einav, Nature Physics **11**, 835 (2015).
[5] N. Vandewalle, Nature Physics **11**, 802 (2015).
[6] T. Barraclough, J. Blackford, S. Liebenstein, S. Sandfeld, T. Stratford, G. Weinlander, and M. Zaiser, Nature Physics **advance online publication** (2016).
[7] A. Portevin and F. Le Châtelier, Comptes Rendus de l'Académie des Sciences **176** (1923).
[8] A. Van den Beukel, Physica status solidi (a) **30**, 197 (1975).
[9] M. A. Lebyodkin, Y. Brechet, Y. Estrin, and L. P. Kubin, Phys. Rev. Lett. **74**, 4758 (1995).
[10] G. D'Anna and F. Nori, Phys. Rev. Lett. **85**, 4096 (2000).
[11] P. Barat, A. Sarkar, P. Mukherjee, and S. K. Bandyopadhyay, Phys. Rev. Lett. **94**, 055502 (2005).
[12] G. Ananthakrishna, Physics Reports **440**, 113 (2007).
[13] H. Halim, D. S. Wilkinson, and M. Niewczas, Acta Materialia **55**, 4151 (2007).
[14] A. Benallal, T. Berstad, T. Børvik, O. S. Hopperstad, and R. Nogueira de Codes, Philosophical Magazine **88**, 3311 (2008).
[15] J. H. Dieterich, Journal of Geophysical Research: Solid Earth **84**, 2161 (1979).
[16] J. Rice and A. Ruina, ASME Journal of Applied Mechanics **50**, 343 (1983).
[17] C. H. Scholz, Nature **391**, 37 (1998).
[18] H. Kawamura, T. Hatano, N. Kato, S. Biswas, and B. K. Chakrabarti, Rev. Mod. Phys. **84**, 839 (2012).
[19] T. Putelat and J. H. Dawes, Journal of the Mechanics and Physics of Solids **78**, 70 (2015).
[20] R. Blumenfeld, Phys. Rev. Lett. **76**, 3703 (1996).
[21] H. Narita, J. Glaciol **26**, 275 (1980).
[22] H. Narita, Contrib. Inst. Low Temp. Sci., Ser. A **32**, 1 (1983).
[23] P. Golshan, (2016).
[24] K. Chihab, Y. Estrin, L. Kubin, and J. Vergnol, Scripta metallurgica **21**, 203 (1987).
[25] T. Lebedkina and M. Lebyodkin, Acta Materialia **56**, 5567 (2008).
[26] A. Yilmaz, Science and Technology of Advanced Materials **12**, 063001 (2011).
[27] C. J. Pérez, Á. Corral, A. Díaz-Guilera, K. Christensen, and A. Arenas, International Journal of Modern Physics B **10**, 1111 (1996).
[28] M. Lebyodkin, N. Kobelev, Y. Bougherira, D. Entemeyer, C. Fressengeas, V. Gornakov, T. Lebedkina, and I. Shashkov, Acta Materialia **60**, 3729 (2012).